PET Imaging of Neutrophil Elastase with ^{11}C-GW457427 in Acute Respiratory Distress Syndrome in Pigs

Emmi Puuvuori[1], Elena Chiodaroli[2], Sergio Estrada[1], Pierre Cheung[1], Norbert Lubenow[3], Jonathan Sigfridsson[4], Hampus Romelin[4], Sofie Ingvast[3], Mathias Elgland[1,4], Francesco Liggieri[2], Olle Korsgren[3], Gaetano Perchiazzi*[2], Olof Eriksson*[1], and Gunnar Antoni*[1,4]

[1]Science for Life Laboratory, Department of Medicinal Chemistry, Uppsala University, Uppsala, Sweden; [2]Hedenstierna Laboratory, Department of Surgical Sciences, Uppsala University, Uppsala Sweden; [3]Department of Immunology, Genetics, and Pathology, Uppsala University, Uppsala, Sweden; and [4]PET Center, Center for Medical Imaging, Uppsala University Hospital, Uppsala, Sweden

Today, there is a lack of clinically available imaging techniques to detect and quantify specific immune cell populations. Neutrophils are one of the first immune cells at the site of inflammation, and they secrete the serine protease neutrophil elastase (NE), which is crucial in the fight against pathogens. However, the prolonged lifespan of neutrophils increases the risk that patients will develop severe complications, such as acute respiratory distress syndrome (ARDS). Here, we evaluated the novel radiolabeled NE inhibitor ^{11}C-GW457427 in a pig model of ARDS, for detection and quantification of neutrophil activity in the lungs. **Methods:** ARDS was induced by intravenous administration of oleic acid to 5 farm pigs, and 4 were considered healthy controls. The severity of ARDS was monitored by clinical parameters of lung function and plasma biomarkers. Each pig was studied with ^{11}C-GW457427 and PET/CT, before and after pretreatment with the NE inhibitor GW311616 to determine in vivo binding specificity. PET image data were analyzed as SUVs and correlated with immunohistochemical staining for NE in biopsies. **Results:** The binding of ^{11}C-GW457427 was increased in pig lungs with induced ARDS (median SUV_{mean}, 1.91; interquartile range [IQR], 1.67–2.55) compared with healthy control pigs ($P < 0.05$ and $P = 0.03$, respectively; median SUV_{mean}, 1.04; IQR, 0.66–1.47). The binding was especially strong in lung regions with high levels of NE and ongoing inflammation, as verified by immunohistochemistry. The binding was successfully blocked by pretreatment of an NE inhibitor drug, which demonstrated the in vivo specificity of ^{11}C-GW457427 ($P < 0.05$ and $P = 0.04$, respectively; median SUV_{mean}, 0.60; IQR, 0.58–0.77). The binding in neutrophil-rich tissues such as bone marrow ($P < 0.05$ and $P = 0.04$, respectively; baseline median SUV_{mean}, 5.01; IQR, 4.48–5.49; block median SUV_{mean}, 1.57; IQR, 0.95–1.85) and spleen (median SUV_{mean}, 2.14; IQR, 1.19–2.36) was also high in all pigs. **Conclusion:** ^{11}C-GW457427 binds to NE in a porcine model of oleic acid–induced lung inflammation in vivo, with a specific increase in regional lung, bone marrow, and spleen SUV. ^{11}C-GW457427 is a promising tool for localizing, tracking, and quantifying neutrophil-facilitated inflammation in clinical diagnostics and drug development.

Key Words: inflammation; PET; neutrophil elastase; ARDS

The acute respiratory distress syndrome (ARDS) is a life-threatening condition characterized by lung injury, infiltration of immune cells, increased permeability, and decreased pulmonary function (1). Inflammation damages the thin-walled alveoli and the alveolar–capillary unit, determining lung edema, decreased lung compliance, and hypoxemia, eventually resulting in the need for mechanical ventilation (2). Different direct (e.g., pneumonia or pulmonary injury) or indirect (e.g., sepsis) mechanisms can lead to ARDS, and despite improvement in treatment, the condition is associated with high mortality (3).

There are several inflammatory biomarkers associated with ARDS, such as cytokines, demonstrating that immune cell recruitment and accumulation are an important path of the pathology (4). Inflammatory processes may affect all major organs and, unresolved, may lead to development of fibrosis and finally organ failure. Even in ARDS induced by intrapulmonary causes such as injurious mechanical ventilation, activation of the inflammatory cascade and mediators carried by the blood circulation can reach remote organs and contribute to multiorgan failure (5).

In this process, immune-active cells such as leukocytes play a key role, and neutrophils are the most abundant leukocytes in the circulation. They are part of the innate immune system, acting as a first line of defense in the immune response, and are recruited to the site of damage within minutes after trauma or acute inflammation. Neutrophils are produced from stem cells in the bone marrow, and they are highly mobile not only in the bloodstream but also in the marginated intravascular pools in the lungs, spleen, and liver (6,7). The lifespan of neutrophils in healthy humans is short, as inactivated neutrophils survive only around 8 h (8). However, the activated neutrophils can prolong their existence up to 5 d (9). The extended life of activated neutrophils promotes chronic inflammation and inflammation-related morbidity in several lung diseases, including ARDS (7,10). On activation, neutrophils can increase the permeability of the blood vessels to proteins and migrate through them into interstitium. Neutrophils can defend the host from invaders by phagocytosis, secretion, and release of antimicrobials (degranulation) and formation of neutrophil extracellular traps (11). One of the biomarkers linked with ARDS is neutrophil extracellular traps, whose purpose is to physically trap microorganisms on the DNA strands to prevent the spread and to disarm pathogens using antimicrobial proteins such as neutrophil elastase (NE) (2).

NE is a serine protease stored in the primary granules of neutrophils and released on neutrophil activation by degranulation and

neutrophil extracellular traps. Thus, NE has a key role in mediating tissue remodeling, but it can also damage the lung parenchyma and the airway walls. NE inhibitors such as sivelestat have been investigated as a treatment for acute lung injury and ARDS, with mixed results and no proven efficacy (12). This could potentially be explained by insufficient dosing, exposure, or duration of treatment. No quantitative molecular imaging modality such as PET and a selective PET tracer targeting NE has been used to verify the interaction between drug and drug target and quantify the degree of elastase inhibition in vivo. Thus, monitoring the potential of these novel therapeutic strategies requires improved understanding and techniques to monitor disease progression noninvasively.

Currently, the NE activity in vivo can be monitored by intravital microscopy, which is limited in depth and field of view and is therefore suitable mainly for preclinical use on small animals (6,13). Clinically, in vitro NE levels can be analyzed from sputum and plasma samples; however, the sputum samples are unreliable and plasma samples are not tissue-specific to lungs.

In vivo imaging of NE activity has also been attempted by radiolabeling of a peptide with high affinity for NE (14). The resulting tracer, ^{99m}Tc-mercaptoacetyltriglycine-EPI-human neutrophil elastase inhibitor 2, could visualize inflammation in tissue in nonhuman primates, demonstrating the feasibility of NE in vivo imaging by SPECT.

^{11}C-GW457427 (0.44 kDa) is a novel small-molecule PET tracer targeting NE. We have recently reported good-manufacturing-practice–ready production, toxicology, dosimetry, metabolite analysis, and in vivo binding data on mice for ^{11}C-GW457427 (15), as well as a pilot clinical study on patients with coronavirus disease 2019 (COVID-19) (16).

The aim of this study was to validate ^{11}C-GW457427 as a PET marker for NE in a translationally relevant large-animal model of ARDS. Porcine and human neutrophils behave similarly and have comparable respiratory mechanics and gas exchange in the lungs (17,18). This makes the pig a relevant model for preclinical studies of NE in ARDS.

MATERIALS AND METHODS

Radiosynthesis of ^{11}C-GW457427

^{11}C-GW457427 was synthesized as described in detail previously (15,16). ^{11}C-GW457427 ($n = 17$) was generated with radiochemical purity of more than 95%.

Animal Handling

The animal experiments were authorized by the Animal Ethics Committee of the Swedish Animal Welfare Agency and performed according to the ARRIVE and institutional guidelines ("Uppsala University Guidelines on Animal Experimentation," UFV 2007/724).

Induction of ARDS in Pig

On the morning of the study day, pigs ($n = 9$; weight, 22–27 kg; Swedish landrace; mean age, 2 mo) were transported to Uppsala University and anesthetized initially by intramuscular administration of tiletamine-zolazepam. Swedish Landrace pigs were chosen because they are a common pig strain in Sweden. Their health is strictly controlled by the veterinarian authorities, but the strain is not genetically modified or the result of inbreeding. The selected age of the pigs was primarily due to logistics, as Swedish Landrace pigs are around 25–30 kg in weight at the age of 2 mo, which is large enough to be suitable for the spatial resolution of the clinical PET scanner used (3–5 mm) but small enough to handle and transport under anesthesia.

Anesthesia was maintained with intravenous ketamine, fentanyl, and midazolam as previously described (19). The experiment was conducted with the animal supine to mimic a patient's position on the intensive care bed. The animals were ventilated in volume-controlled mode, with an inspired oxygen fraction of 0.5, positive end-expiratory pressure of 5 cm H_2O, tidal volume of 6 mL/kg, and respiratory rate of 20/min. Minute volume was adjusted to maintain normocapnia during the experiment by titrating the respiratory frequency. Acute lung damage was induced in 5 pigs by injection of oleic acid (cis-9-octadecenoic acid, OA) as described previously in detail (20,21). Approximately a 0.1 mL/kg dose of OA-ethanol solution (1:1 by volume) was given. OA-ethanol solution was administered through a central venous catheter in repeated boluses of around 0.5 mL. Particular attention was paid to obtaining a complete dispersion of the OA into the infusate, avoiding large droplets. Administration of OA was suspended if O_2 saturation fell below 80%. Any fall in systemic arterial pressure during OA injection was countered using epinephrine, in boluses of 0.01 mg.

Of the 9 pigs in this study, 5 had induced lung inflammation and 4 were untreated. The lung function and severity of the ARDS were evaluated by repeatedly monitoring ventilator readouts (in particular lung compliance) and the partial pressure of arterial blood gases together with the oxygen saturation of arterial hemoglobin and the ratio between partial pressure of oxygen in arterial blood and inspired oxygen fraction. The measurements were conducted before the ARDS induction (baseline), directly after ARDS (T1), after the first injection of ^{11}C-GW457427 (T2), and after the administration of blocking compound (T3).

Whole-blood and plasma samples were also acquired at these time points, for analysis of standard peripheral markers at the hospital clinical chemistry core lab. Blood samples were also acquired for thromboelastography analysis of coagulation efficiency. The viscoelastic properties were analyzed using the TEG 6s platform (Haemonetics) (22), analyzing coagulation in citrated whole blood, generating the parameters reaction time (R-time), angle, maximal amplitude, and percentage lysis at 30 min.

^{11}C-GW457427 PET/CT Imaging of Pigs with ARDS

An attenuation CT scan (100 kV; 80–400 mA; noise index, 10; rotation, 1.27 cm [0.5 in]; full spiral; slice thickness, 3.75 mm; pitch, 0.98:1; reconstructed diameter, 50 mm) was initially attained using a digital 4-ring, 64-slice scanner with a 198-mm axial field of view. Afterward, ^{11}C-GW457427 (10 MBq/kg, corresponding to around 3–5 µg of substance) was injected, and a 60-min dynamic PET (Discovery MI; GE Healthcare) scan (4-mm spatial resolution; 30 frames: 12 × 10 s, 6 × 30 s, 5 × 2 min, 5 × 5 min, and 2 × 10 min) was simultaneously started over the lungs. A 30-min static scan over the spleen was immediately started after the dynamic study. Both scans were repeated after intravenous pretreatment with a 1 mg/kg dose of NE inhibitor GW311616 (a 1 mL/kg dose of a 1 mg/mL concentration of GW311616 in 0.9% NaCl), administered as a slow bolus 20 min before the tracer, approximately 2 h after the first injection. The dose of inhibitor (1 mg/kg) was based on the dosing used previously in mice (15) and was around 5,000 times higher than the tracer mass dose (in the range of 0.1–0.2 µg/kg).

The baseline scan was started approximately 2.5 h and the blocking scan 4.5 h after the OA treatment was initiated. Radioactivity in arterial plasma and whole blood was determined during the dynamic scans at 5, 30, and 60 min after injection with a γ-well counter. Lastly, a contrast-enhanced CT scan was acquired by late arterial (17 s) and venous phase contrast-enhanced CT (70 mL of iohexol [Omnipaque; GE Healthcare], 350 plus 40 mL of NaCl, 3.5 mL/s, bolus tracking on the descending aorta, threshold of 100 Hounsfield units [HUs]). The PET images were reconstructed using an iterative VPFX-S algorithm (GE Healthcare; ordered-subsets expectation maximization, time of

flight, resolution recovery: 3 iterations, 16 subsets, 3-mm postprocessing filter, and 256 × 256 matrix).

After the PET scans, each pig was euthanized by intravenous KCl under deep anesthesia. Biopsies were taken from the lung (right and left, apical and basal parts), spleen, and liver, both for snap freezing and for fixation in formalin for immunohistochemical staining.

PET/CT Pig Image Data Analysis

The volumes of interest were manually segmented over the lungs as previously described in detail (23), on SUV-corrected coronal projections using PMOD software (PMOD Technologies LLC). No further kinetic modeling of PET data was performed, because of the lack of assessment of arterial metabolites in the pigs. The HU values over the lungs were obtained from CT images using the same segmentations. In addition, bone and muscle volumes of interest were delineated on dynamic images, and time–activity curves were defined on all organs. The data were summarized and illustrated on Prism (GraphPad Software Inc.) and presented as median and interquartile range (IQR). Baseline, blocking, and control groups were tested for normality by Shapiro–Wilk testing, and since not all groups were normally distributed, the relationship among groups was assessed by Mann–Whitney U testing, where P values of less than 0.05 were considered significant.

Histology of Pig Biopsies

Postmortem formalin-fixed and paraffin-embedded biopsy samples of the lungs and spleen were acquired after the PET studies and processed into 6-μm sections. Sections were immunostained for NE using an anti-NE antibody (ab68672, rabbit polyclonal; Abcam) in a concentration of 1 μg/mL. Bound antibody was visualized by Dako EnVision and diaminobenzidine-based substrate (K4065, Agilent) according to the manufacturer's instructions. Sections were counterstained with hematoxylin, dehydrated, mounted, and analyzed by light microscopy (Leica). Pig spleen sections were used as positive controls, and negative controls had the primary antibody replaced by buffer. Consecutive sections from pig lung and spleen were also stained by sirius red and hematoxylin and eosin according to the routine at the local hospital pathology department (Uppsala University Hospital).

RESULTS

Visual ^{11}C-GW457427 Uptake in ARDS Pigs Compared with Control

NE infiltration was assessed using ^{11}C-GW457427 on pigs after lung damage, in comparison with healthy animals. PET/CT images (from 30 to 60 min after administration), as well as time–activity curves, displayed distinct uptake of ^{11}C-GW457427 in the lungs of pigs with induced ARDS (Figs. 1A and 1E), which was abolished in the second scan by pretreatment with an NE inhibitor (Figs. 1B and 1F). Conversely, lung uptake in control pigs was negligible (Figs. 1C, 1D, 1G, and 1H). Binding of ^{11}C-GW457427 in the lung was consistent with positive immunostaining for NE in the lung from pigs with induced ARDS (Supplemental Fig. 1; supplemental materials are available at http://jnm.snmjournals.org). Binding of ^{11}C-GW457427 in the bone marrow was visible in both ARDS and control pigs, and the binding could be blocked by pretreatment with an NE inhibitor (Figs. 1A–1H).

Lung Binding of ^{11}C-GW457427 and ARDS Severity Assessment

On the more damaged dorsal parts, uptake of ^{11}C-GW457427 was significantly higher at baseline (median SUV$_{mean}$, 1.91; IQR, 1.67–2.55) than after preblocking ($P < 0.05$ and $P = 0.04$, respectively; median SUV$_{mean}$, 0.60; IQR, 0.58–0.77) or in control pigs ($P < 0.05$ and $P = 0.03$, respectively; median SUV$_{mean}$, 1.04;

IQR, 0.66–1.47) at 60 min after injection (Fig. 2A). The uptake on the ventral parts was also significantly higher at baseline (median SUV$_{mean}$, 0.76; IQR, 0.63–0.98) than with blocking ($P < 0.05$ and $P = 0.04$, respectively; median SUV$_{mean}$, 0.32; IQR, 0.27–0.47) but not between ARDS and healthy control pigs ($P = 0.41$; median SUV$_{mean}$, 0.66; IQR, 0.47–0.89) (Fig. 2A). The successful induction of ARDS was confirmed by continuous monitoring of lung function (Fig. 2B; Supplemental Table 1). The ratio between partial pressure of oxygen in arterial blood and inspired oxygen fraction decreased with time, dropping below 100 mm Hg at T2, confirming the presence of severe ARDS according to the Berlin definition (1). Oxygen saturation dropped longitudinally, being significantly different between baseline and T3 ($P < 0.05$ and $P = 0.02$, respectively) (Fig. 2B). The damage was also evident in the quantitative analysis of the CT scans (Fig. 2C), with the most dorsal parts of the lungs exhibiting an average density of -63.52 HU, compared with the control dorsal (-495.52 HU), baseline ventral (-528.00 HU), and control ventral (-652.20 HU) parts. Common clinical chemistry laboratory markers were also measured in repeated blood samples from each pig, where changes in peripheral markers were inconclusive (Supplemental Fig. 2). Thromboelastography results under the experiment's duration showed no evidence of coagulopathy, with no significant differences between the ARDS group and control at baseline (Supplemental Fig. 3). Histologic staining for NE, hematoxylin and eosin, and sirius red in tissue biopsy samples taken after death further demonstrated severe inflammation in the lung of the ARDS group, as well as NE-positive cells in the spleen (Supplemental Fig. 1).

The plasma–to–whole-blood ratio for ^{11}C-GW457427 was examined in all pigs throughout the dynamic studies. The plasma-to-blood ratio was below 1 in both ARDS-induced pigs and control pigs after injection of tracer alone and decreased over time (Supplemental Fig. 4A). After preblocking with a pharmacologic dose of an NE inhibitor, the ratio was instead above 1 and was stable over the course of the PET scan in both ARDS and control pigs. This finding indicates more ^{11}C-GW457427 available in plasma for tissue distribution after pretreatment with the inhibitor.

Whole-Body Distribution and Binding of ^{11}C-GW457427

The biodistribution seen in the static whole-body scans from 60 to 90 min after ^{11}C-GW457427 injection supported the finding for the dynamic PET scan. Strong ^{11}C-GW457427 binding was seen on both maximum-intensity projections (Figs. 3A–3B) and coronal projections (Supplemental Figs. 4B–4C) in hemopoietic tissues with a known presence of neutrophils, including spleen, peripheral blood (here measured as heart ventricle), and bone marrow. Importantly, binding in these tissues was decreased after inhibition of NE (Figs. 3B–3C; Supplemental Fig. 4C). The presence of NE in pig spleen (median SUV$_{mean}$, 2.14; IQR, 1.19–2.36) was also verified by immunohistochemistry of paraffin-embedded biopsy samples (Supplemental Fig. 1). For example, uptake in the bone marrow was significantly blocked ($P < 0.05$ and $P = 0.04$, respectively; baseline median SUV$_{mean}$, 5.01; IQR, 4.48–5.49; block median SUV$_{mean}$, 1.57; IQR, 0.95–1.85) in the ARDS model, and binding to bone marrow in control animals (baseline median SUV$_{mean}$, 3.89; IQR, 2.49–4.23) was similar in magnitude to that in ARDS pigs. Muscle uptake remained unchanged at the background level (baseline median SUV$_{mean}$, 0.29; IQR, 0.27–0.34). Uptake in kidneys, liver, and muscle was unaffected, consistent with nonspecific uptake due to excretion or background blood contribution to the signal.
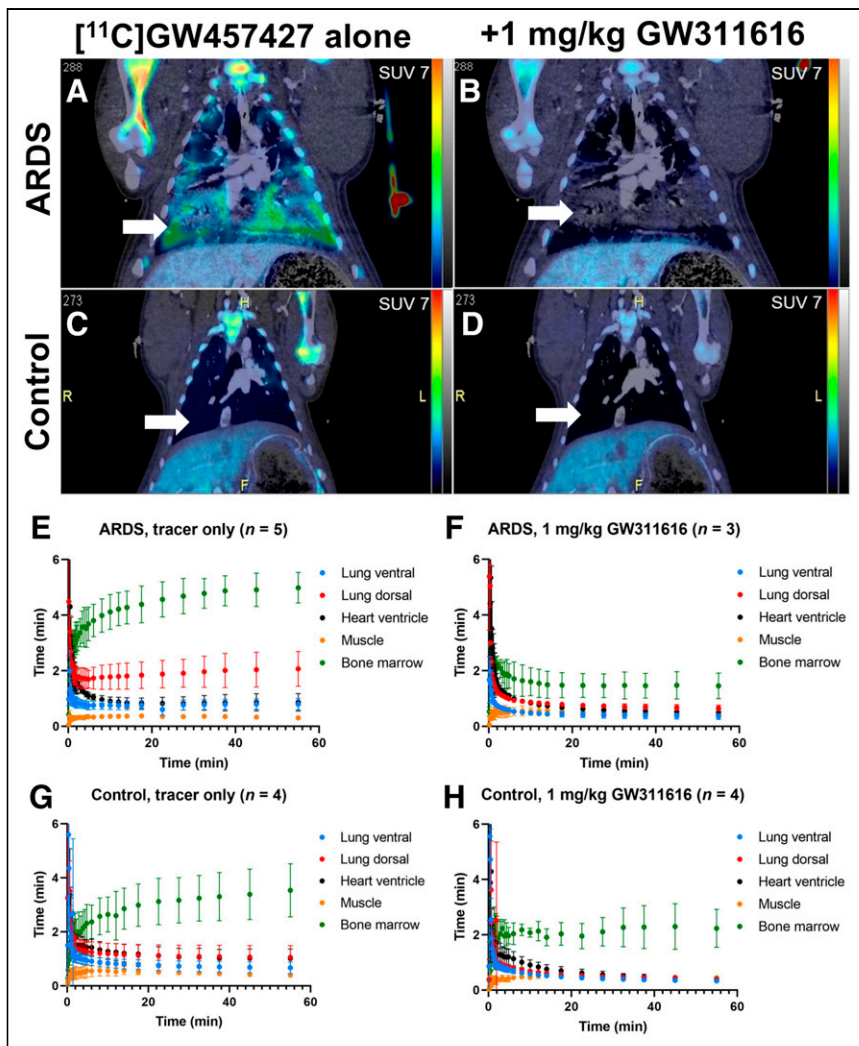
FIGURE 1. (A–D) Representative coronal PET/CT images of ARDS (A and B) and control (C and D) pigs after administration of ^{11}C-GW457427 alone or after pretreatment with NE inhibitor GW311616. Arrows indicate lungs, and SUV scale bar is from 0 to 7. PET images are summed frames from 30 to 60 min after tracer administration. (E–H) Averaged time–activity curves showing distribution and binding of ^{11}C-GW457427 in pigs with induced ARDS (E and F) and control pigs (G and H).
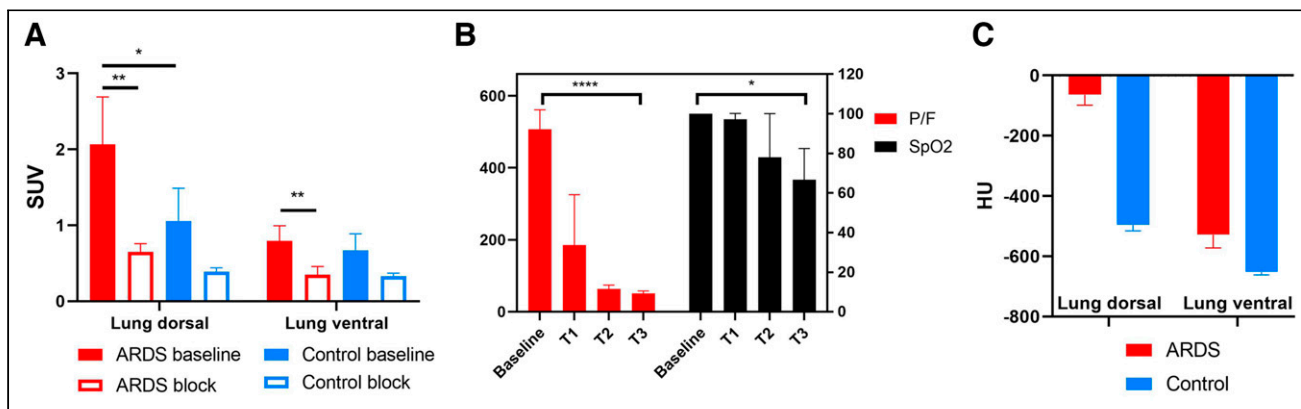
DISCUSSION

In this study, we validated use of the novel radiotracer ^{11}C-GW457427 for targeting NE in a large-animal model of lung inflammation and ARDS. Neutrophils are the first cells migrating to the lungs during inflammation, and their activation changes the lung pathology by releasing inflammatory mediators and molecules, such as NE. We demonstrated that uptake of ^{11}C-GW457427 in an oleic acid–induced lung inflammation pig model was strong, specific, and reproducible.

In both healthy and ARDS-induced pigs, uptake of ^{11}C-GW457427 was heterogeneously distributed and higher in the more damaged dorsal (gravitationally dependent during the experiment) parts of the lungs. The spread of damage follows the distribution of lung circulation (24) and is supported by HU analysis and histology. In fact, both oleic acid and neutrophils are carried predominantly to the dependent, better-perfused areas of the lung, where it is possible to observe the multifocal and heterogeneous alterations typical of ARDS (25,26). Since the lung injury models also cause permeability changes and vessel leakage, the risk for nonspecific uptake gathering in the lungs is always present. However, in this study we were able to block uptake of ^{11}C-GW457427, indicating the specificity of the binding and making us conclude that the dependent, dorsal areas of the lung are the real battleground where the inflammatory reaction takes place. The used tidal volumes, falling in the range of the so-called protective ventilation (27), make us exclude a role of ventilator-induced lung injury (28) in the present experiment.

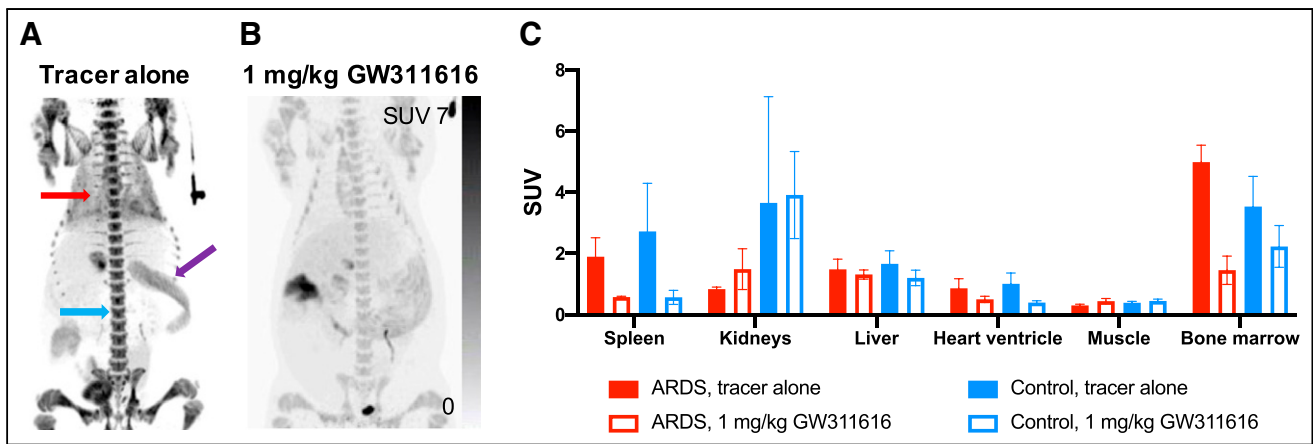In addition to the lungs, other organs of interest in this study consisted of hemopoietic

FIGURE 2. (A) Binding of ^{11}C-GW457427 in lung regions in ARDS and control pigs. (B) Lung function over time in ARDS group before ARDS induction (baseline), directly after ARDS induction (T1), after injection of ^{11}C-GW457427 (T2), and after administration of blocking (T3). (C) Damage in lungs in ARDS model was clearly visible on CT and was further confirmed by quantifying lung tissue density by CT.

FIGURE 3. Representative images from whole-body scan acquired from 60 to 90 min after ^{11}C-GW457427 administration. (A and B) Maximum-intensity projections for baseline (A) and blocking (B) scans of same pig. Red arrow indicates lung, purple arrow indicates spleen, and blue arrow indicates bone marrow. (C) Bar graph showing binding of ^{11}C-GW457427 in tissues in both ARDS and control pigs during baseline scan or after blocking. Displaceable binding was found in spleen, heart ventricle, and bone marrow.

tissues such as bone marrow and spleen. Since neutrophils are produced in the bone marrow, we expected to see uptake there as well as in the spleen because of the previously described accumulation in the marginated intravascular pools. Uptake was similar in ARDS and control pigs and could be abolished, to a large extent, by pretreatment with the selective NE inhibitor GW311616.

Furthermore, we noticed binding in the blood pool, both by observing the signal in the heart ventricle (estimation of blood concentration) and by measuring the plasma and whole-blood content of radioactivity in blood samples. During the baseline scan, when only ^{11}C-GW457427 was administered, there was a plasma–to–whole-blood ratio lower than 1, which decreased with time. This means that more ^{11}C-GW457427 was present in the cellular components than was free in plasma. After preblocking with GW311616, the plasma–to–whole-blood ratio increased to above 1 and was stable during the PET examination, indicating more tracer available in the plasma component. This was apparent both in the ARDS and in the control groups. We hypothesize that these observations are due to binding of ^{11}C-GW457427 to intracellular NE in circulating neutrophils. The sum of data in hemopoietic tissue spleen, bone marrow, and peripheral blood thus indicates that ^{11}C-GW457427 can cross the cell membrane of both activated and quiescent neutrophils and bind the intracellular pool of NE stored in granules. Such an NE-specific binding in circulating neutrophils could also explain the weakly blockable signal observed also in the lung of control pigs, for example; this signal is at least partially due to neutrophils continually passing though the tissue via the blood.

Analysis of time-dependent uptake in tissues from the dynamic scan showed that uptake remained stable in the lungs in ARDS but increased slowly in bone marrow during the scan. NE in circulating quiescent neutrophils and in the bone marrow is stored in highly condensed granules and is less accessible for binding to ^{11}C-GW457427 than is NE that has been released extracellularly to the tissue after activation or degranulation of the neutrophils at the site of inflammation. The kinetics of binding of ^{11}C-GW457427 to extracellular, easily accessible NE will likely be significantly faster than the kinetics of binding of ^{11}C-GW457427 to stored intracellular NE. To bind intracellular NE, ^{11}C-GW457427 must diffuse through 2 membranes (both the cell and the granule membranes); in addition, accessibility to the active site of NE might

be reduced by packing or storage of the enzyme in the granules. This hypothesis would explain the difference in uptake kinetics (time–activity curve) of radioactivity in lung from that in bone marrow. Additionally, the observation of increased whole-blood–to–plasma ratio with time, in the baseline scans, also fits this hypothesis. Furthermore, we have preliminary data demonstrating that ^{11}C-GW457427 binds NE both in intact and in homogenized neutrophils (Puuvuori et al., unpublished data, March 1, 2022). Thus, ^{11}C-GW457427 will bind both to extracellular activated NE and to inactivated NE inside neutrophils at the site of inflammation. This is important information for correct interpretation of clinical ^{11}C-GW457427 PET images, as it will be challenging to separate extracellular NE from neutrophils at sites of inflammation. Further development to decrease the ability of ^{11}C-GW457427 to diffuse across the cell membrane, such as by increasing hydrophilicity, may lead to a PET tracer more specific for extracellular NE.

In lungs affected by ARDS and inflammation, uptake is rapid and steady—in accordance with a fast on-rate of binding due to the accessibility of NE. In the bone marrow, on the other hand, overall kinetics are slower and increase during the scan, as is in accordance with an apparent slower on-rate of binding driven by the lower intracellular accessibility of the target enzyme.

Previously, ^{18}F-FDG was proposed as a potential marker to assess neutrophilic recruitment in the lungs in inflammatory conditions. Even though neutrophils contribute to the increased uptake of ^{18}F-FDG in lung inflammation, ^{18}F-FDG is inherently nonspecific and will also accumulate in other activated immune cells with increased metabolism, such as macrophages, lymphocytes, and eosinophils. The structural cells in the lungs also increase glucose consumption throughout inflammation, contributing to the increased ^{18}F-FDG uptake. Therefore, ^{18}F-FDG imaging represents the combined inflammatory response during lung inflammation and cannot reliably be used to measure changes in specific immune cell populations, such as neutrophilic accumulation in response to, for example, antiinflammatory treatments (*29,30*). ^{11}C-GW457427 belongs to a class of selective NE inhibitors originally developed as immunomodulatory drugs. NE is highly specific for neutrophils, and ^{11}C-GW457427 is thus likely to bind to other types of immune cells, such as macrophages.

The performance of ^{11}C-GW457427 in a large-animal model of ARDS is in accordance with previous data on rodents (*15*). In that

study, strong lung binding of ^{11}C-GW457427 was seen in mice after lipopolysaccharide induction of lung inflammation, which could be blocked by coinjection of a 1 mg/kg dose of unlabeled GW457427. Elevated signal was also found in the spleen and bone marrow, although not to the same extent as in pigs. The pig data presented here are furthermore in line with the first-in-humans results of ^{11}C-GW457427, with strong binding in inflammatory lesions in the lungs of individuals with COVID-19 but not controls (16). Additionally, strong binding was seen in the spleen and bone marrow in both groups, as in pigs. The pig model has the added benefit of allowing intervention by preadministration of an NE inhibitor to demonstrate the specificity of ^{11}C-GW457427. Thus, the in vivo data presented here expand on previous preclinical studies and assist in interpretation of available and future clinical studies on ^{11}C-GW457427.

Limitations of the current study were related mainly to the experimental design and to the restrictions on logistics imposed by the pig model. The strength of the experimental design is that it allows direct comparison between binding of the PET tracer in lung before and after blocking with an NE inhibitor, in each individual. The drawback is instead that postmortem assessment is available only after administration of inhibitor. Furthermore, the complexity and cost of the model, and its combination with the PET scanning, mean that the number of repeated examinations in each group is relatively low ($n = 3–5$). Finally, the pigs are relatively young and thus may not accurately recapitulate all aspects of the immune response in human adult ARDS.

In the future, ^{11}C-GW457427 might potentially be used to demonstrate the pathophysiology of damage distribution during ventilation-induced lung injury and patient self-induced lung injury (which is still lacking direct morphofunctional proofs) (31) or to monitor the response to neutrophil-targeting therapeutics during acute inflammation, such as COVID-19 treatments in drug development (32). In fact, the recently reported first-in-humans clinical study using ^{11}C-GW457427 did indeed demonstrate strong binding in the lung of individuals with active COVID-19, indicating that NE inhibitors may be a potential treatment strategy given the ample amount of NE in the inflammatory lesions. Neutrophils have also been found to accumulate in several types of tumors, making ^{11}C-GW457427 a potentially attractive noninvasive technique to further elucidate the role of neutrophils and NE in immune oncology (33,34).

CONCLUSION

[11]C-GW457427 showed significantly higher uptake in a pig model of ARDS lung inflammation than in healthy pigs in vivo using PET. The specificity of ^{11}C-GW457427 binding to NE was verified by blocking studies with an NE inhibitor. ^{11}C-GW457427 is a promising and noninvasive tool for localizing, tracking, and quantifying neutrophil-mediated inflammation in clinical diagnostics and drug development.

DISCLOSURE

ACKNOWLEDGMENTS

KEY POINTS

QUESTION: Can ^{11}C-GW457427 be used to image NE in a large-animal model?

PERTINENT FINDINGS: The preclinical evaluation of ^{11}C-GW457427 uptake in a pig lung inflammation model was consistent, reproducible, and specific. Uptake in lung in pigs with ARDS was significantly increased compared with healthy control animals and could be abolished by preblocking.

IMPLICATIONS FOR PATIENT CARE: ^{11}C-GW457427 is a novel PET tracer for in vivo imaging of NE—a crucial part of the innate immune system—in inflammatory diseases.

REFERENCES

1. Ranieri VM, Rubenfeld GD, Thompson BT, et al.; ARDS Definition Task Force. Acute respiratory distress syndrome: the Berlin definition. *JAMA.* 2012;307:2526–2533.
2. Matthay MA, Zemans RL, Zimmerman GA, et al. Acute respiratory distress syndrome. *Nat Rev Dis Primers.* 2019;5:18.
3. Bellani G, Laffey JG, Pham T, et al; LUNG SAFE Investigators; ESICM Trials Group. Epidemiology, patterns of care, and mortality for patients with acute respiratory distress syndrome in intensive care units in 50 countries. *JAMA.* 2016;315: 788–800.
4. Matthay MA, Ware LB, Zimmerman GA. The acute respiratory distress syndrome. *J Clin Invest.* 2012;122:2731–2740.
5. Plötz FB, Slutsky AS, van Vught AJ, Heijnen CJ. Ventilator-induced lung injury and multiple system organ failure: a critical review of facts and hypotheses. *Intensive Care Med.* 2004;30:1865–1872.
6. Silvestre-Roig C, Hidalgo A, Soehnlein O. Neutrophil heterogeneity: implications for homeostasis and pathogenesis. *Blood.* 2016;127:2173–2181.
7. De Filippo K, Rankin SM. The secretive life of neutrophils revealed by intravital microscopy. *Front Cell Dev Biol.* 2020;8:603230.
8. Summers C, Rankin SM, Condliffe AM, Singh N, Peters AM, Chilvers ER. Neutrophil kinetics in health and disease. *Trends Immunol.* 2010;31:318–324.
9. Gramegna A, Amati F, Terranova L, et al. Neutrophil elastase in bronchiectasis. *Respir Res.* 2017;18:211.
10. Williams AE, Chambers RC. The mercurial nature of neutrophils: still an enigma in ARDS? *Am J Physiol Lung Cell Mol Physiol.* 2014;306:L217–L230.
11. Klopf J, Brostjan C, Eilenberg W, Neumayer C. Neutrophil extracellular traps and their implications in cardiovascular and inflammatory disease. *Int J Mol Sci.* 2021; 22:1–17.
12. Iwata K, Doi A, Ohji G, et al. Effect of neutrophil elastase inhibitor (sivelestat sodium) in the treatment of acute lung injury (ALI) and acute respiratory distress syndrome (ARDS): a systematic review and meta-analysis. *Intern Med.* 2010;49: 2423–2432.
13. Fisher DT, Muhitch JB, Kim M, et al. Intraoperative intravital microscopy permits the study of human tumour vessels. *Nat Commun.* 2016;7:10684.
14. Rusckowski M, Qu T, Pullman J. at al. Inflammation and infection imaging with a ^{99m}Tc-neutrophil elastase inhibitor in monkeys. *J Nucl Med.* 2000;41:363–374.
15. Estrada S, Elgland M, Selvaraju RK, et al. Preclinical evaluation of [^{11}C]GW457427 as a tracer for neutrophil elastase. *Nucl Med Biol.* 2022;106–107:62–71.

16. Antoni G, Lubberink M, Sörensen J, et al. In vivo visualization and quantification of neutrophil elastase in lungs of COVID-19 patients: a first-in-human positron emission tomography study with ^{11}C-GW457427. *J Nucl Med.* June 9, 2022 [Epub ahead of print].

17. Bréa D, Meurens F, Dubois AV, et al. The pig as a model for investigating the role of neutrophil serine proteases in human inflammatory lung diseases. *Biochem J.* 2012;447:363–370.

18. Monteiro A, Smith RL. Bronchial tree architecture in mammals of diverse body mass. *Int J Morphol.* 2014;32:312–318.

19. Perchiazzi G, Rylander C, Derosa S, et al. Regional distribution of lung compliance by image analysis of computed tomograms. *Respir Physiol Neurobiol.* 2014;201: 60–70.

20. Matute-Bello G, Frevert CW, Martin TR. Animal model of acute lung injury. *Am J Physiol Lung Cell Mol Physiol.* 2008;295:L379–L399.

21. Perchiazzi G, Rylander C, Pellegrini M, Larsson A, Hedenstierna G. Monitoring of total positive end-expiratory pressure during mechanical ventilation by artificial neural networks. *J Clin Monit Comput.* 2017;31:551–559.

22. Dias JD, Haney EI, Mathew BA, Lopez-Espina CG, Orr AW, Popovsky MA. New-generation thromboelastography: comprehensive evaluation of citrated and heparinized blood sample storage effect on clot-forming variables. *Arch Pathol Lab Med.* 2017;141:569–577.

23. Puuvuori E, Liggieri F, Velikyan I, et al. PET-CT imaging of pulmonary inflammation using [68Ga]Ga-DOTA-TATE. *EJNMMI Res.* 2022;12:19.

24. Glenny RW, Robertson HT. Spatial distribution of ventilation and perfusion: mechanisms and regulation. *Compr Physiol.* 2011;1:375–395.

25. Gonçalves-de-Albuquerque CF, Silva AR, Burth P, et al. Acute respiratory distress syndrome: role of oleic acid-triggered lung injury and inflammation. *Mediators Inflamm.* 2015;2015:260465.

26. Kamuf J, Garcia-Bardon A, Ziebart A, et al. Oleic acid-injection in pigs as a model for acute respiratory distress syndrome. *J Vis Exp.* 2018;2018:1–8.

27. Brower RG, Matthay MA, Morris A, Schoenfeld D, Thompson BT, Wheeler A; Acute Respiratory Distress Syndrome Network. Ventilation with lower tidal volumes as compared with traditional tidal volumes for acute lung injury and the acute respiratory distress syndrome. *N Engl J Med.* 2000;342:1301–1308.

28. Slutsky AS, Ranieri VM. Ventilator-induced lung injury. *N Engl J Med.* 2013;369: 2126–2136.

29. Aulakh GK, Kaur M, Brown V, Ekanayake S, Khan B, Fonge H. Quantification of regional murine ozone-induced lung inflammation using [18F]F-FDG microPET/ CT imaging. *Sci Rep.* 2020;10:15699.

30. Scherer PM, Chen DL. Imaging pulmonary inflammation. *J Nucl Med.* 2016;57: 1764–1770.

31. Brochard L, Slutsky A, Pesenti A. Mechanical ventilation to minimize progression of lung injury in acute respiratory failure. *Am J Respir Crit Care Med.* 2017;195: 438–442.

32. Reusch N, De Domenico E, Bonaguro L, et al. Neutrophils in COVID-19. *Front Immunol.* 2021;12:652470.

33. Uribe-Querol E, Rosales C. Neutrophils in cancer: two sides of the same coin. *J Immunol Res.* 2015;2015:983698.

34. Powell DR, Huttenlocher A. Neutrophils in the tumor microenvironment. *Trends Immunol.* 2016;37:41–52.